








Bridging between the Integrated and Resolved Main Sequence of Star Formation

Shoubaneh Hemmati¹ , Bahram Mobasher², Hooshang Nayyeri³ , Abtin Shahidi², Peter Capak⁴ , Behnam Darvish⁴ ,
Nima Chartab² , Marziye Jafariyazani², and Zahra Sattari²

¹Jet Propulsion Laboratory, California Institute of Technology, Pasadena, CA 91109, USA; shemmati@caltech.edu

²University of California Riverside, 900 University Avenue, Riverside, CA 92521, USA

³University of California Irvine, Irvine, CA 92697, USA

⁴California Institute of Technology, 1200 East California Boulevard, Pasadena, CA 91125, USA

Received 2019 December 3; revised 2020 January 24; accepted 2020 February 3; published 2020 June 11

Abstract

The position of galaxies on the stellar mass, star formation rate (SFR) plane with respect to the star-forming main sequence at each redshift is a convenient way to infer where the galaxy is in its evolution compared to the rest of the population. We use Hubble Space Telescope high-resolution images in the GOODS-S field from the the Cosmic Assembly Near-IR Deep Extragalactic Legacy Survey (CANDELS) and fit multiwavelength lights in resolution elements of galaxies with stellar population synthesis models. We then construct resolved kpc-scale stellar mass, SFR surface density curves for galaxies at $z \sim 1$. Fitting these resolved main sequence curves with Schechter functions, we parameterize and explain the multiwavelength structure of galaxies with three variables: ϕ^* , α , and M^* . For quenched galaxies below the main sequence, we find an average high-mass slope (α) of the resolved main sequence curves to be ~ -0.4 . The scatter of this slope is higher among the lower mass star-forming galaxies and those above the main sequence compared to quenched galaxies, due to lack of an evolved bulge. Our findings agree well with an inside-out quenching of star formation. We find that the knee of the Schechter fits (M^*) for galaxies below the main sequence occurs at lower stellar mass surface densities compared to star-forming galaxies, which hints at how far quenching has proceeded outward.

Unified Astronomy Thesaurus concepts: [Galaxies \(573\)](#); [Star formation \(1569\)](#); [Galaxy quenching \(2040\)](#); [Galaxy structure \(622\)](#); [Galaxy bulges \(578\)](#); [Dynamical evolution \(421\)](#); [Astrostatistics \(1882\)](#); [Galaxy evolution \(594\)](#)

1. Introduction

The past 13 billion years witnessed a vast evolution from tiny quantum fluctuations to the wide variety of galaxy structures and shapes that we observe today. Studies of scaling relations among the physical properties of galaxies and their evolution with cosmic time have not only been critical in shaping our current understanding of galaxy formation and evolution (e.g., Faber & Jackson 1976; Tully & Fisher 1977), but are as well a magnificent aid in reducing systematics in cosmology (e.g., Huff & Graves 2014)

One such scaling relation is the tight correlation between the star formation rate (SFR) and stellar mass in star-forming galaxies (i.e., star-forming main sequence) out to high redshifts (e.g., Lilly et al. 2013; Speagle et al. 2014; Salmon et al. 2015), with the bulk of star formation occurring primarily in massive star-forming galaxies as compared to less massive systems (e.g., Noeske et al. 2007; Bell et al. 2005; Reddy et al. 2006). A population of passive galaxies also exists and lies below the main sequence, whereas starbursts lie above. The slope of the main sequence is almost constant at each epoch but the zero-point evolves significantly with time. The cause of the evolution in the main sequence is not very well understood. There is also discrepancy among the slope and scatter around the relation reported in different studies using different SFR diagnostics and various sample selections.

With the ever-increasing wealth of high-resolution observations, we have, however, entered a new era that moves beyond studying galaxies as single data points and into one that systematically probes resolved properties of large samples of galaxies (e.g., Guo et al. 2012; Wuyts et al. 2012; Hemmati et al. 2014, 2015; Ellison et al. 2020). In this Letter, we explore the resolved star formation surface density versus stellar mass

surface density plane of $z \sim 1$ galaxies and its relation to the integrated star-forming main sequence. Section 2 introduces the sample and data used in this work. In Section 3 we explain the method used to measure the resolved main sequence for individual galaxies (i.e., star formation surface density versus stellar mass surface density). The bridge between the resolved main sequence and the integrated SFR-stellar mass plane is presented in Section 4. Finally in Section 5, we address and discuss sources of uncertainty. Throughout this Letter all magnitudes are expressed in AB system (Oke & Gunn 1983) and we use standard cosmology with $H_0 = 70 \text{ km s}^{-1} \text{ Mpc}^{-1}$, $\Omega_M = 0.3$, and $\Omega_\Lambda = 0.7$.

2. Sample

Galaxies for this study are selected from the GOODS-S field where science-ready deep multiband high-resolution optical and near-infrared (near-IR) Hubble Space Telescope (HST) images from the Cosmic Assembly Near-IR Deep Extragalactic Legacy Survey (CANDELS; Grogin et al. 2011; Koekemoer et al. 2011) exist. We use images in four optical pass bands from the Advanced Camera for Survey (ACS): F435W, F606W, F775W, and F850lp as well as three from the Wide Field Camera 3 (WFC3): F105W, F125W, and F160W.

CANDELS also publicly provides catalogs (Guo et al. 2013 in the GOODS-S) of multiwaveband photometries along with estimates of integrated physical properties of galaxies (e.g., redshifts, sizes, stellar masses, SFRs). We focus our studies here on $z \sim 1$ galaxies, where the HST observations cover rest-frame ultraviolet (UV) to near-IR wavelengths and hence, can provide reliable estimates of the resolved physical properties. This redshift regime is also optimal for our aim because while the star-forming main sequence of galaxies at $z \sim 1$ is well in

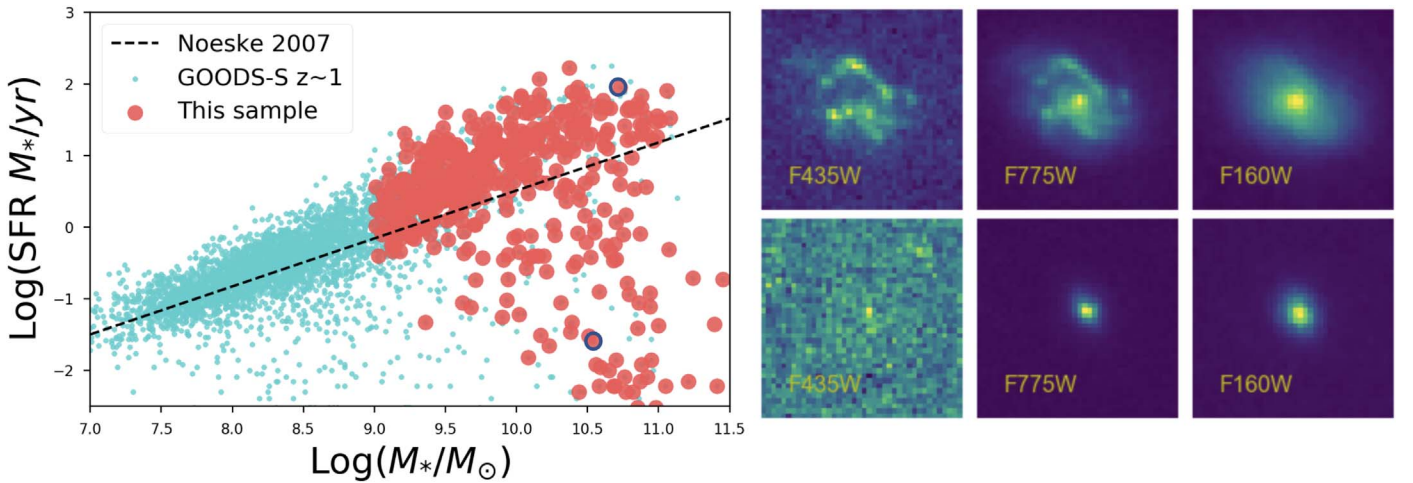


Figure 1. Left panel: galaxies selected for this study are shown as red circles on top of all GOODS-S galaxies at $z \sim 1$ shown with cyan dots. Black dashed line shows the main sequence of star-forming galaxies at this redshift from Noeske et al. (2007). Right panels: HST cutouts in F435W, F775W, and F160W of a star-forming and quenched galaxy on top and bottom panels, respectively.

place and well studied there are also plenty of galaxies below the main sequence to study statistically.

In the left panel of Figure 1, we present the sample selected for this work on top of all $z \sim 1$ galaxies in the GOODS-S field on the SFR-stellar mass plane. Both stellar mass and SFR here are taken from the public CANDELS catalogs. In addition to our selection cut of stellar mass ($>10.0^9 M_*/M_\odot$) and redshift ($0.8 < z < 1$), we also remove elongated galaxies ($b/a > 0.5$) and those fainter than 26 AB mag in the F160W and we only include galaxies with spectroscopic redshifts. This leaves us with 545 galaxies. We show HST cutouts in F435W, F775W, and F160W filters for two galaxies (a star-forming galaxy on top and a passive galaxy on the bottom) from the sample in the right panels of Figure 1.

3. Resolved Main Sequence

To measure resolved properties for the galaxies in our sample from the HST images, we follow the same steps outlined in Hemmati et al. (2014), using an improved and now fully automated python pipeline (see, e.g., Jafariyazani et al. 2019). The pipeline makes large 100×100 pixel cutouts from the seven HST bands centered on the R.A. and decl. of each sample galaxy, where each pixel in the image corresponds to $0''.06$. The resolution of the shorter wavelength cutouts are then matched to the resolution of F160W, using the convolution method in *astropy* and a matching kernel created by the *photutils* package using the point-spread functions (PSFs) of HST images. The initial large size of the cutouts is selected to remove issues due to PSF matching near edges of the cutouts. After PSF matching smaller cutouts of 40×40 pixels are regenerated, which correspond to a physical scale of ~ 20 kpc at $z \sim 1$. To make the pixel photometric catalog per galaxy we mask background pixels surrounding the galaxy using a segmentation routine that we wrote and fine tuned to find edges of galaxies. We used image processing modules from the *SciPy.ndimage* in the segmentation maker routine.

Given the pixel-based photometric catalogs, we fit for the resolved kiloparsec-scale physical properties at each resolution element with the LePhare (Arnouts et al. 1999; Ilbert et al. 2006) spectral energy distribution (SED) fitting code. We use the Bruzual and Charlot (Bruzual & Charlot 2003) stellar

population synthesis models, a Chabrier initial mass function (Chabrier 2003), exponentially declining or τ model star formation histories, sub-solar stellar metallicity, and the Calzetti dust attenuation curve (Calzetti et al. 2000) to build the library of model SEDs. The justification for these choices in building the model library and the effect of modifications to these assumptions is fully discussed in Hemmati et al. (2014). There, we also performed tests of accuracy of the resolved SED-fitting measurements by comparing integrated and sum of resolved measured values.

The best-fitting model representing resolved galaxy photometries is found and used by LePhare to assign stellar mass surface densities and SFR surface densities to individual resolution elements in all galaxies in our sample. Figure 2 shows the SFR surface density versus the stellar mass surface density or the so-called resolved main sequence of star formation for four sample galaxies color coded with distance of the resolution element from the center of each galaxy.

The shapes of the resolved main sequence curves are very informative about the physical properties of galaxies. Stellar mass surface density increases toward smaller distances from the center of the galaxy. SFR surface density also mostly increases from the outer disks toward the center but with decreasing slopes. It is important to keep in mind that both stellar mass and SFR surface densities are fit with the same SED fitting code and models and hence the tightness of these curves can be partly due to the dependence of both on the library of model SEDs used to fit for these physical properties. However, each resolution element is fit independently of the others and the tight distributions observed are mostly due to gradual change of photometry from one resolution element to the next.

The general shape of the resolved main sequence is rising in low stellar mass densities, reaches a peak, and falls toward massive pixels located in the center of galaxies. This shape can be parameterized with a Schechter function (1), which is typically used to fit the luminosity or mass function of galaxies.

$$\text{SF}(m_*) = \phi^* \times 10^{(M^* - m_*)(\alpha + 1)} \times e^{-10^{(M^* - m_*)}} \quad (1)$$

In Equation (1), SF and m_* are the SFR and stellar mass surface densities, respectively. We used *scipy.curvefit* with bounds on possible values to fit for the three free parameters:

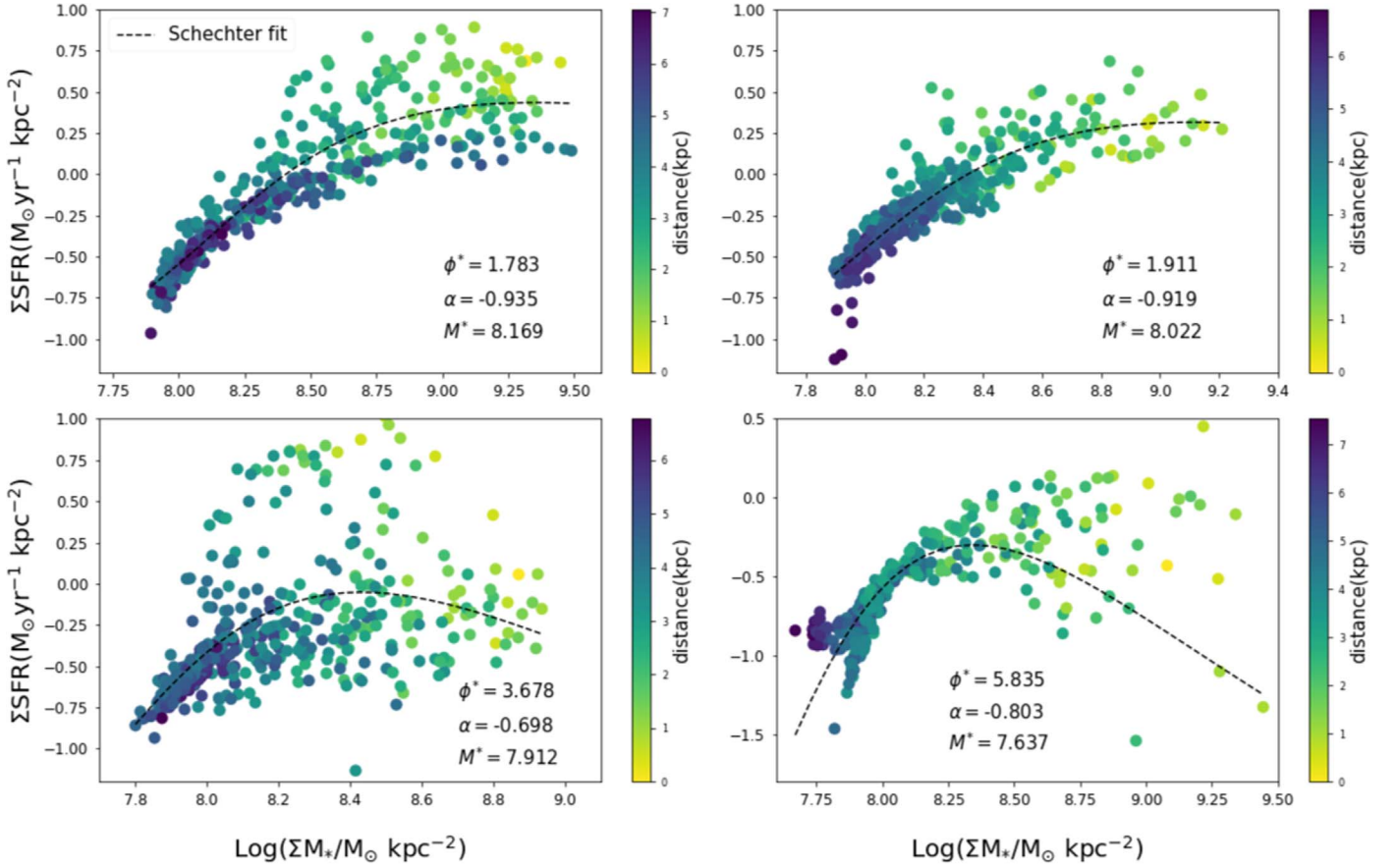


Figure 2. Resolved star formation surface density vs. stellar mass surface density plots of four sample galaxies color coded by distance from the center. Dashed black lines show the best Schechter function fit to data.

ϕ^* the normalization factor, α the high-mass slope, and M^* the characteristic mass or the knee of the resolved main sequence. The best-fit Schechter functions and their parameters are also shown in Figure 2 for the four sample galaxies.

4. The Bridge

Location on the integrated SFR– M_* plane with respect to the main sequence of star-forming galaxies at each redshift is a simple way to infer how far each individual galaxy is in its evolution. For instance, Scoville et al. (2017), based on multi-variable model fitting bins galaxies out to high redshift on integrated SFR– M_* planes, studied star formation efficiencies and interstellar medium mass estimates from Atacama Large Millimeter/submillimeter Array (ALMA) submillimeter observations as a function of distance from the star-forming main sequence. Here, we adopt a similar strategy and bin our sample on the integrated SFR– M_* plane to study how the shape of the resolved main sequence curves vary across this plane.

The left three columns of Figure 3 show the median (top row) and standard deviation (bottom row) of best-fit Schechter parameters in bins of stellar mass and SFR. We have excluded galaxies with poor Schechter fits. We calculated the goodness of fit using the diagonal elements of the covariance matrix of parameters measured by *curvefit*. We also exclude bins with only one galaxy. The bottom-right panel of Figure 3 shows the number of galaxies in each bin. The integrated star-forming main sequence at $z \sim 1$ (Noeske et al. 2007) is over plotted on all panels (red solid line).

The median of ϕ^* is lower for galaxies on and above the star-forming main sequence compared to the galaxies below the star-forming main sequence. ϕ^* increases smoothly at each fixed stellar mass bin with decreasing SFR and at fixed SFR bins, with increasing stellar mass. The standard deviation of ϕ^* , however, does not show dependence on location with respect to the star-forming main sequence.

The variation in α values is not as clear as ϕ^* . As can be seen from the $\sigma\alpha$ plot the variation is lower in the higher mass end of the main sequence compared to lower mass bins. This can be explained by the evolution of the central bulge of galaxies toward higher masses. More massive galaxies have more evolved bulges, with the highest stellar mass surface densities. By definition evolved bulges have lower specific SFRs compared to a less evolved bulge. α or the high stellar mass surface density slope of the Schechter function corresponds to the spread of the pixels in the central parts of the galaxy where the bulges form. If most resolution elements have high stellar mass and low SFR surface densities, scatter of α is low and if some pixels are still forming stars at higher rates then the bulge is not fully evolved and scatter is large. Our results show that the scatter of α is low at higher mass galaxies, meaning the central parts of these galaxies are more settled compared to lower mass galaxies, where either the bulge has not fully formed yet or the star formation is still ongoing in some of the resolution elements. The presence of an evolved bulge imposes strong constraint on the high-mass end of the Schechter functions. The high $\sigma\alpha$ values above the main sequence, also point to the increased scatter in their resolved main sequence

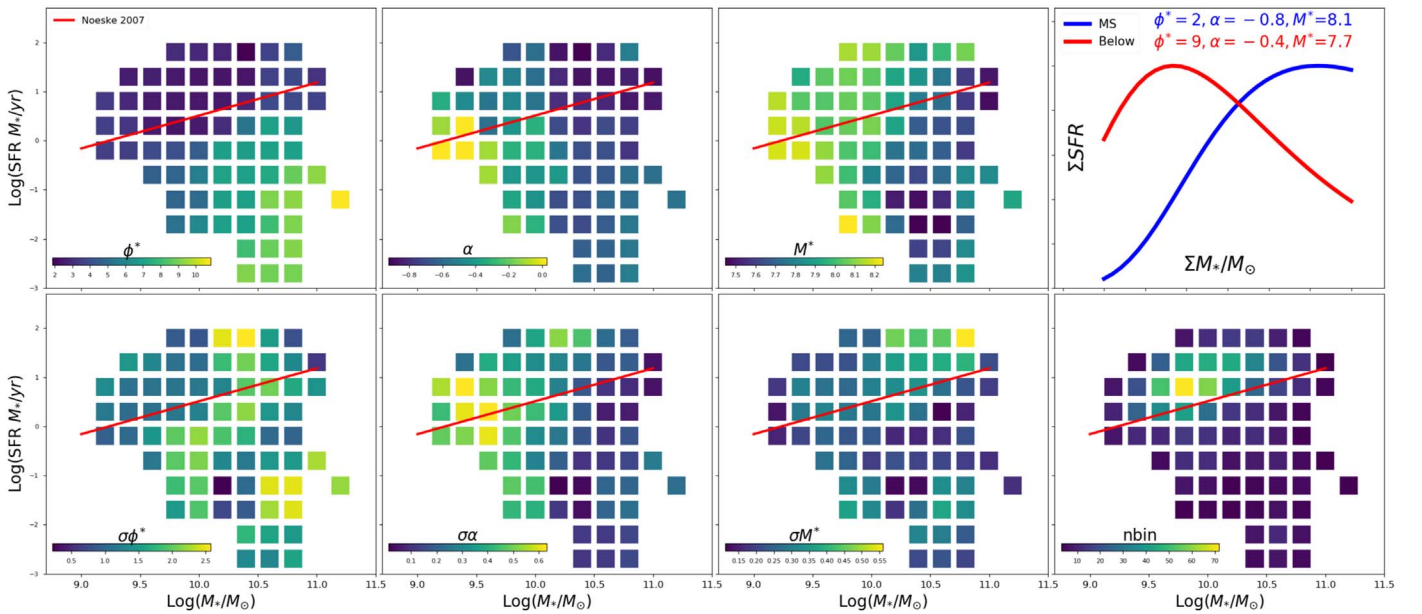


Figure 3. Schechter parameters best fitted to the resolved main sequence of star formation of individual galaxies are shown on the binned integrated stellar mass-SFR plane. The three left columns show the median (top row) and standard deviation (bottom row) of ϕ^* , α , and M^* . Red solid line shows the main sequence of star-forming galaxies at $z \sim 1$ to guide the eye. The top-right panel shows two Schechter functions with average value of galaxies on and two dex below the main sequence at $\text{Log}(M_*/M_\odot) \sim 10.5$. The bottom-right panel shows number of galaxies in each bin of SFR and stellar mass.

curves at higher stellar mass surface densities, which in addition to lack of an evolved bulge can be possibly due to presence of more star-forming clumps in these systems. At fixed stellar mass bins however, an increase in α is seen as SFR decreases.

The third column of Figure 3 shows variation of M^* across the bins of stellar mass and SFR. A clear decrease of M^* diagonally from low mass and high SFR to high mass and low SFR distance indicates that the Schechter function breaks in lower characteristic masses in more massive and evolved systems. The average scatter of M^* in bins is ~ 0.3 dex and the maximum reaches 0.5 dex in the bin with the highest integrated stellar mass and SFR.

The top-right panel of Figure 3 summarizes the plot by showing an average shape (with normalized y-axis) of the resolved main sequence curve for galaxies (at $\text{Log}(M_*/M_\odot) \sim 10.5$) on and below the main sequence.

5. Discussion

Comparison of the Schechter fits to resolved main sequence curves on and below the integrated star-forming main sequence points toward an inside-out quenching of star formation. The more quiescent galaxies below the main sequence have their knee of the Schechter fit at lower masses and quenching is pushed toward outer radii. Our findings in this Letter conform well with previous literature linking the inside-out quenching to the growth of the central bulge (e.g., Fang et al. 2013; Hemmati 2015; Tacchella et al. 2015; Jafariyazani et al. 2019; Morselli et al. 2019).

Here, we used the Schechter function to fit the resolved main sequence curves for the first time. Similar to the literature on luminosity functions, one concern can be why Schechter functions are chosen and not double power laws or other functional forms. Here, the aim was to investigate whether and how the shape of the resolved main sequence informs us about its integrated properties, specifically its position with regards to

the main sequence of star formation and whether it is quenched. Schechter function parameters, i.e., the faint end slope (here the high-mass slope), the knee or the characteristic luminosity/mass/magnitude, and the normalization are well known by the astronomy community and very easy to visually interpret.

We have also excluded sources with poor Schechter fits from the final analysis. Apart from the possibility of intrinsically distinct structural profiles in a small subset of targets (e.g., active galactic nuclei, mergers), large errors in some of the Schechter fits can be due to imperfections/failures in various steps of the automated measurement (e.g., segmentation mask, resolved SED-fitting on low surface brightness resolution elements). Here, the sample is being trimmed based on curve fitting error rather than in the beginning based on stellar mass surface density and signal-to-noise ratio of pixels. Choosing the cut value is not straightforward. Having a low fitting error threshold ($E < 0.25$) results in removing 80% of objects, with the majority of the remaining galaxies being massive and star-forming. Changing this threshold to a very large value ($E < 20$) results in removing only 10% of objects from the sample, 98% of which are less massive than $\text{log}(M_*/M_\odot) = 9.75$. $E < 5$ removes 18% of galaxies as poor fits, with 97% of them being less massive than 9.75. We chose galaxies with ($E < 1.5$) removing 30% of the sample, 92% of which being galaxies with $\text{log}(M_*/M_\odot) < 9.75$. The exact value of the cut is arbitrary; however, with the chosen value the fits visually represent the overall spread of data on the M_* -SFR plane well. Moreover, the trends in Figure 3 are there regardless of this choice. The trends only get clearer where better fits are kept and having a moderate value of 1.5 ensures enough statistics.

The resolved main sequence curves also clarify to some extent, the scatter around the main sequence of star formation. Given which galaxies end up in a given sample, the more bulge-dominated ones will bring the integrated measure down while the star-forming clumps within a disk will push the whole thing up. We note here again the dependence of the

stellar mass and SFR surface density on the model library used for fitting the SED of each resolution element. The continuity of the shapes seen in the resolved curves, depend on parameter steps used in defining the model library. This is because the photometry is changing rather smoothly in kpc-scale at $z \sim 1$ galaxies with changing radius. One may use an independent measurement of the resolved SFR to improve upon this analysis. This can be done using hydrogen Balmer lines observed with integral field spectrographs to measure dust corrected SFR from $H\alpha$ and $H\beta$. Future work is also needed to extend this analysis to a broader redshift range and study the evolution of star formation in galaxies. The high spatial resolution and longer wavelength coverage of the James Webb Space telescope makes it an optimal choice for this purpose.

We wish to thank the referee for providing very useful suggestions and recommendations. S.H. is thankful to A. Pagul for careful reading of this manuscript and for constructive comments. B.D. acknowledges financial support from the National Science Foundation, grant No. 1716907. Parts of this research were carried out at the Jet Propulsion Laboratory, California Institute of Technology, under a contract with the National Aeronautics and Space Administration.

ORCID iDs

Shoubaneh Hemmati  <https://orcid.org/0000-0003-2226-5395>

Hooshang Nayyeri  <https://orcid.org/0000-0001-8242-9983>

Peter Capak  <https://orcid.org/0000-0003-3578-6843>

Behnam Darvish  <https://orcid.org/0000-0003-4919-9017>

Nima Chartab  <https://orcid.org/0000-0003-3691-937X>

References

- Arnouts, S., Cristiani, S., Moscardini, L., et al. 1999, *MNRAS*, 310, 540
 Bell, E. F., Papovich, C., Wolf, C., et al. 2005, *ApJ*, 625, 23
 Bruzual, G., & Charlot, S. 2003, *MNRAS*, 344, 1000
 Calzetti, D., Armus, L., Bohlin, R. C., et al. 2000, *ApJ*, 533, 682
 Chabrier, G. 2003, *PASP*, 115, 763
 Ellison, S. L., Thorp, M. D., Lin, L., et al. 2020, *MNRAS Letters*, 493, L39
 Faber, S. M., & Jackson, R. E. 1976, *ApJ*, 204, 668
 Fang, J. J., Faber, S. M., Koo, D. C., & Dekel, A. 2013, *ApJ*, 776, 63
 Grogin, N. A., Kocevski, D. D., Faber, S. M., et al. 2011, *ApJS*, 197, 35
 Guo, Y., Ferguson, H. C., Giavalisco, M., et al. 2013, *ApJS*, 207, 24
 Guo, Y., Giavalisco, M., Ferguson, H. C., Cassata, P., & Koekemoer, A. M. 2012, *ApJ*, 757, 120
 Hemmati, S. 2015, PhD thesis, Univ. California, Riverside
 Hemmati, S., Miller, S. H., Mobasher, B., et al. 2014, *ApJ*, 797, 108
 Hemmati, S., Mobasher, B., Darvish, B., et al. 2015, *ApJ*, 814, 46
 Huff, E. M., & Graves, G. J. 2014, *ApJL*, 780, L16
 Ilbert, O., Arnouts, S., McCracken, H. J., et al. 2006, *A&A*, 457, 841
 Jafariyazani, M., Mobasher, B., Hemmati, S., et al. 2019, *ApJ*, 887, 204
 Koekemoer, A. M., Faber, S. M., Ferguson, H. C., et al. 2011, *ApJS*, 197, 36
 Lilly, S. J., Carollo, C. M., Pipino, A., Renzini, A., & Peng, Y. 2013, *ApJ*, 772, 119
 Morselli, L., Popesso, P., Cibinel, A., et al. 2019, *A&A*, 626, A61
 Noeske, K. G., Weiner, B. J., Faber, S. M., et al. 2007, *ApJL*, 660, L43
 Oke, J. B., & Gunn, J. E. 1983, *ApJ*, 266, 713
 Reddy, N. A., Steidel, C. C., Fadda, D., et al. 2006, *ApJ*, 644, 792
 Salmon, B., Papovich, C., Finkelstein, S. L., et al. 2015, *ApJ*, 799, 183
 Scoville, N., Lee, N., Vanden Bout, P., et al. 2017, *ApJ*, 837, 150
 Speagle, J. S., Steinhardt, C. L., Capak, P. L., & Silverman, J. D. 2014, *ApJS*, 214, 15
 Tacchella, S., Carollo, C. M., Renzini, A., et al. 2015, *Sci*, 348, 314
 Tully, R. B., & Fisher, J. R. 1977, *A&A*, 500, 105
 Wuyts, S., Förster Schreiber, N. M., Genzel, R., et al. 2012, *ApJ*, 753, 114